A Correction Method for Thermal Deformation Positioning Error of Geostationary Optical Payloads

Xiaoyan Li, Lin Yang, Xiaofeng Su, Zhuoyue Hu, and Fansheng Chen

***Abstract*— Geometric positioning of a remote sensing image is one of the core technologies for the quantitative application of the geostationary satellite data. Affected by the change of the incident angle of the sunlight, the spatial thermal environment surrounding the remote sensing cameras (RSCs), especially the geostationary RSCs, fluctuates greatly and has a noticeable impact on the installation matrix based on the reference to the satellite body. Therefore, the spatial thermal environment will ultimately influence the camera's geometric positioning model and the final positioning accuracy. This paper proposes a novel correction method based on stellar observations for correcting geometric positioning error caused by spatial thermal deformation (STD) of geostationary optical payloads. The proposed method overcomes the drawbacks associated with current stabilization methods that involve shutting down the camera to reduce STD effects. Experimental results show that the positioning error corrected by the proposed method can be within ±1.9 pixels (2σ) at a 95% confidence level and better than the ±18 pixels before correction.**

***Index Terms*— Error correction, geometric positioning model (GPM), spatial thermal deformation (STD).**

I. Introduction

GEOSTATIONARY orbiting remote sensing cameras (RSCs) have been widely used in the fields of earth observation and space surveillance. Indeed, earth imaging from geostationary orbit provides new functionalities not covered by low earth orbit observation missions, such as real-time monitoring and fast revisit capability of any location within the field of regard of the satellite. Geostationary RSCs offer a good complement to those images produced by low-orbit missions in disaster monitoring, such as floods, large landslides, and storms [1]–[3]. With the improvement in the resolution of spatial RSCs, image navigation and registration technology have been broadly applied to the field of remote sensing image geometric positioning [4]–[6]. However, the geometric positioning model of high-orbit RSCs changes gradually because of the effects of vibration deformation resulting from satellite launch and spatial thermal deformation (STD) caused by the change of the incident angle of sunlight. Such changes in the geometric positioning model are able to affect the final positioning accuracy of the cameras. Therefore, typically the RSCs are frequently re-calibrated in-orbit [7]–[11]. At present, there are few studies on the optimum correction method in correcting positioning errors caused by STD.

The operational temperature of low-orbit satellites, especially polar sun-synchronized satellites, is much more stable (±0.5°) than that of high-orbit satellites, so STD has only a subtle effect on optical payload positioning accuracy of low-orbit satellites. The distortions of the Satellite Pour l'Observation de la Terre 4-HRV1 (High Resolution Visible) sensors mostly result from the mechanical strain produced when the satellite was launched rather than from the effects of on-orbit thermal variations, namely, the STD, or aging [12], [13]. In addition to the calibration errors of internal and external orientation parameters, the geometric positioning error of RSCs mainly derives from image distortion caused by satellite platform jitter and attitude fluctuation [14]–[16]. Without the correction for STD, the geometric pointing accuracy of the ZiYuan-3 (ZY-3) stereo mapping satellite with bundle block adjustment can achieve 3.5 pixels and 1.8 pixels in planimetry and elevation, respectively, without ground control points (GCPs), and 1.5 pixels and 0.8 pixels in planimetry and elevation, respectively, with high-accuracy GCPs [17]–[19].

The operational temperature experienced by geostationary orbit satellites changes dramatically (±12°) compared to low-orbit satellites, and therefore, the resulting STD will leave a considerably detrimental impact on the camera's geometric positioning accuracy. In terms of the geostationary orbit satellites, there have been some efforts in the design phase to avert or correct the positioning error caused by STD. In order to constrain the fluctuation of the thermal environment within the satellite to be less than 0.5 K, the Chinese GaoFen4 (GF-4) remote sensing satellite adopts corrective methods by the shutdown of the optical payload to reduce the positioning error caused by STD during a period of severe solar radiation. After geometric calibration on-orbit, the positioning accuracy of GF-4 with relatively few GCPs is demonstrated to be better than 1.0 pixel for both the panchromatic and

Manuscript received November 29, 2018; revised February 28, 2019 and April 16, 2019; accepted May 11, 2019. Date of publication June 12, 2019; date of current version September 25, 2019. This work was supported by the CASEarth Minisatellite Thermal Infrared Spectrometer Project of the Shanghai Institute of Technical Physics, Chinese Academy of Sciences under Grant XDA19010102. *(Corresponding author: Fansheng Chen.)*

X. Li and Z. Hu are with the Shanghai Institute of Technical Physics, Chinese Academy of Sciences, Shanghai 200083, China, and also with the University of Chinese Academy of Sciences, Beijing 100049, China (e-mail: xiaoyanLee2018@163.com; uestchu@163.com).

L. Yang, X. Su, and F. Chen are with the Key Laboratory of Intelligent Infrared Perception, Shanghai Institute of Technical Physics, Chinese Academy of Sciences, Shanghai 200083, China (e-mail: pieroyang@163.com; fishsu@mail.sitp.ac.cn; cfs@mail.sitp.ac.cn).

Color versions of one or more of the figures in this article are available online at http://ieeexplore.ieee.org.

Digital Object Identifier 10.1109/TGRS.2019.2917716

near-infrared sensor and the intermediate infrared sensor [20]–[22]. Although this method ensures a stable thermal environment and diminishes the positioning error caused by STD, the satellite's available operating time is curtailed to 8 h per day, which can hardly meet the demand for long-term continuous observation.

Solar illumination of the interior of the telescope of GeoOculus Satellites, and in particular the primary pointing mirror, is avoided by a sun avoidance maneuver when the Sun angle reaches 30°, i.e., $+/-2$ h around midnight at equinoxes. Although this interrupts the imaging sequence, especially limiting to infrared bands during night time, the telescope is protected against solar energy and cold space by a baffle. In addition, the focal plane and external structures are insulated by multi-layer insulation [23].

In order to effectively suppress the influence of solar stray-light radiation and external thermal flux on the detector and avoid the space constraint of the rocket fairing during the launching phrase, the geosynchronous earth orbit satellites of the Space-Based Infrared System (SBIRS-GEO) adopt a large deployable light shade which is approximately 5 m long and 2 m wide to protect the sensitive sensors from direct sunlight [24], [25]. Although the sunshield contributes to reducing the effect of solar stray-light radiation and external thermal flux on the detector, the tracking motion of the sunshield requires precise integration with the satellite attitude control devices and the corresponding ground control system, which definitely increases the movement instability of the satellite in-orbit as well as the cost and complexity of the subsequent image processing.

The primary instrument on Geostationary Operational Environmental Satellites-R (GOES-R) series satellites is the Advanced Baseline Imager which is located on the thermally isolated earth-pointed platform and has demanding thermal constraints. A scan shroud assembly protects the internal instrument structure from direct solar loading through the optical port during the times in the orbit when solar energy enters the internal instrument cavity. In addition, loop heat pipes interface with an oversized radiator that works together to transfer excess thermal energy from the instrument to space. The radiator creates a sink with an effective temperature of 205 K when exposed to the Sun at a $+/-24°$ angle. With a filtering algorithm and image motion compensation, the absolute navigation accuracy of the Advanced Baseline Imager of GOES-R is approximately 20 μrad (3σ) [26], [27]. In summary, although evading the direct solar radiation can reduce the influence of STD partially and achieve higher positioning accuracy, it inevitably shortens the observing time of the satellite, which can hardly meet the demand for long-term continuous observation for high-orbit satellites.

In this paper, we propose a novel correction method based on the stellar observations for mitigating geometric positioning error caused by STD for geostationary optical payloads. The corrected error of this method can be within ± 1.9 pixels (2σ) at a 95% confidence level. Section II elaborates on the stellar-based geometric positioning model (S-BGPM) and the proposed correction method for a geostationary orbit camera payload. Section III focuses on demonstrating the effectiveness of this proposed method with on-orbit observation data. Finally, conclusions and the prospect for the future work are presented in Section IV.

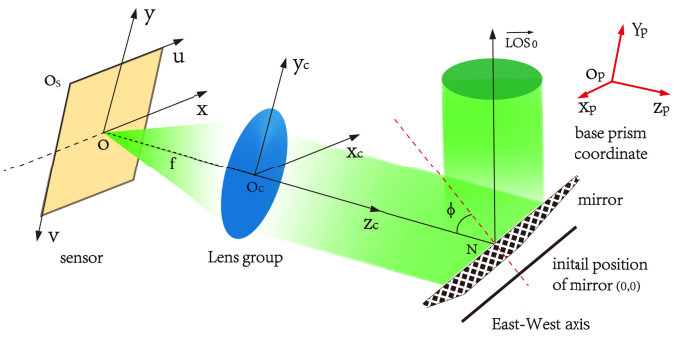

Fig. 1. Schematic of the imaging system of RSCs.o_s_uv is the pixel coordinate system, o_xy is the image coordinate system, $O_{C-}x_Cy_CZ_C$ is the camera coordinate system, $O_{P-}X_PY_PZ_P$ is the basic prism coordinate system.

II. Proposed Positioning Model and Correction Method

A. Stellar-Based Geometric Positioning Model

The S-BGPM of a geostationary orbit camera is comprised mainly of the interior orientation model (IOM) and the exterior orientation model (EOM).

1) Interior Orientation Model: The IOM helps to convert the pixel coordinate system to the camera coordinate system, which allows the determination of the accurate line-of-sight (LOS) of each detector in the camera coordinate system [20].

As shown in Fig. 1, on the sensor focal plane, we define the top left corner as the origin of the pixel coordinate system and the downward and the right direction to be the increasing direction of v-axis, and u-axis, respectively. The x- and y-axes of the image coordinate system are parallel to the x_c-and, y_c-axes of the camera coordinate system, respectively. The origin o is the intersection of the optical axis and the image plane, f is the focal length of the optical system, O_C is the optical center of the camera, ϕ is the intersection angle of the optical axis and the normal of the mirror, and the z_c-axis coincides with the optical axis. $\overrightarrow{\mathrm{LOS}_0}$ is the exit vector corresponding to the principle point of the camera. Then, the exit vector of any pixel in the detector array can be expressed as

$$\overrightarrow{\mathrm{LOS}} = R_{\mathrm{Ref}}(\phi)\cdot R_\theta \cdot R_\varphi \cdot \begin{bmatrix} d_x & 0 & 0 \\ 0 & d_y & 0 \\ 0 & 0 & -f \end{bmatrix} \cdot \begin{bmatrix} u-u_0 \\ v-v_0 \\ 1 \end{bmatrix} \quad (1)$$

where $\overrightarrow{\mathrm{LOS}}$ is the camera's exit vector corresponding to the image point (u, v); $R_{\mathrm{Ref}}(\phi)$ is the reflection matrix of the pointing mirror and ϕ is the intersection angle of the optical axis and the normal of the mirror; R_θ, R_φ are the transformation matrices of the reflection matrix with the pointing mirror's elevation angle θ and the azimuth angle φ, respectively; (u_0, v_0) is the coordinate of the principle point; f is the focal length; and d_x and d_y are the pixel dimensions.

Optical distortion is ubiquitous in the process of design, manufacture, and installation of optical instruments. The existence of distortion is not negligible for high-precision quantitative applications. According to distortion theory [28], [29], if the actual image point's coordinates in the image coordinate system are (x', y') and the distortion model is D(x, y), then we have

$$\begin{cases} x' = x + D_x(x, y) \\ y' = y + D_y(x, y) \end{cases} \tag{2}$$

where (x', y') and (x, y) are the actual and ideal image point coordinates in the image coordinate system; $D_x(x, y)$ and $D_y(x, y)$ are the components of the distortion model in the x- and y- directions, respectively.

Currently, the standard ten-term distortion model comprising interior orientation parameters; lens distortion coefficients and terms for differential scaling and non-orthogonality of the image coordinate axes, are often employed in performing the distortion in the focal plane, as described by Remondino *et al.* [29], Fraser [30]. Although this model can approximate the distortion in the focal plane efficiently and shows impressive accuracy, it is not easy to estimate the parameters precisely with least squares adjustments that are not robust estimation techniques, as incorrect observations can lead to completely incorrect results and might even prevent convergence of the adjustment [31].

In consideration of applications in the engineering field, especially the rapid response and operability, the improved -2-D Lagrange interpolation method is employed to correct the optical distortion in this paper [4] as

$$\begin{cases} x_C = \sum_{j=1}^{n} \sum_{i=1}^{m} \prod_{k=1,k\neq i}^{m} \dfrac{x - x_{ik}}{x_{ij} - x_{ik}} \prod_{l=1,l\neq j}^{n} \dfrac{y - y_{lj}}{y_{ij} - y_{lj}} X_{ij} \\ y_C = \sum_{j=1}^{n} \sum_{i=1}^{m} \prod_{k=1,k\neq i}^{m} \dfrac{x - x_{ik}}{x_{ij} - x_{ik}} \prod_{l=1,l\neq j}^{n} \dfrac{y - y_{lj}}{y_{ij} - y_{lj}} Y_{ij} \end{cases} \tag{3}$$

where x_{ij} and y_{ij} are the actual coordinates of the sample point in i row and j column of the focal plane, X_{ij} and Y_{ij} are the ideal coordinates of the sample points in i row and j column of the focal plane, x and y are the actual coordinates of the image points, and x_C and y_C are the coordinates corrected with the Lagrange interpolation method corresponding to x and y.

2) Exterior Orientation Model: The EOM helps to convert the camera coordinate system to the celestial coordinate system by determining the LOS from the projection center to the object points in the celestial coordinate system.

In Fig. 2, the camera is mounted on the satellite platform with three declination angles α, β, and γ relative to the three axes of the satellite body coordinate system. The conversion of the camera coordinate system to the satellite body coordinate system is performed by the installation matrix $R_{C2S}(\alpha, \beta, \gamma)$. O_S is the centroid of the satellite in the satellite body coordinate system. The X_S-axis points in the flight direction of the satellite, the Y_S-axis is along the satellite horizontal axis, and the Z_S-axis is determined according to the right-hand rule. The origin O_O of the orbital coordinate system is located in the centroid of the satellite. X_O-axis points in the

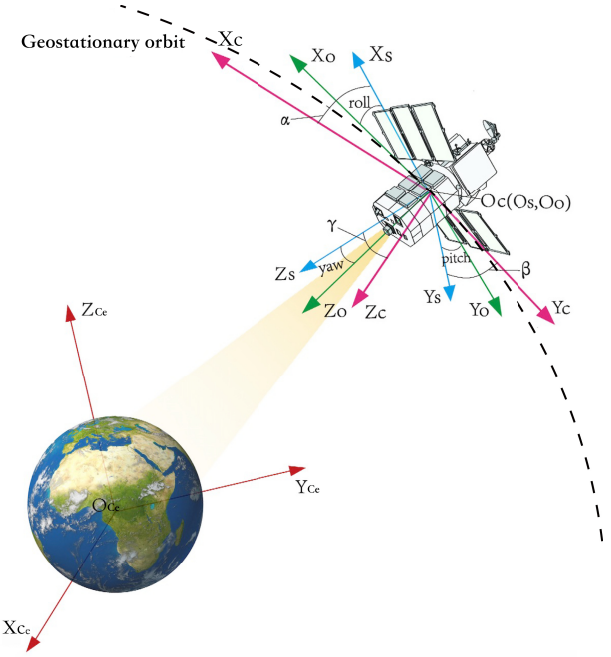

Fig. 2. Illustration of the coordinate's conversion. $O_{C-}x_C y_C Z_C$ is the camera coordinate system, $O_{S\_}X_S Y_S Z_S$ is the satellite body coordinate system, $O_{O-}X_O Y_O Z_O$ is the orbital coordinate system, and $O_{Ce-}X_{Ce}Y_{Ce}Z_{Ce}$ is the celestial coordinate system.

direction of satellite motion in the orbital plane, the Z_O-axis points to the center of the earth, and Y_O-axis is determined by the right-hand rule. The conversion between the satellite body coordinate system and the orbital coordinate system is represented by $R_{S2O}(\text{pitch}, \text{roll}, \text{yaw})$ which is comprised of three attitude angles pitch, roll, and yaw. The transformation matrix R_{O2Ce} between the orbital coordinate system and the celestial coordinate system depends on the instantaneous position vector and velocity vector of the satellite [32]. Given $\vec{P}(t)$ and $\vec{V}(t)$ represent the instantaneous position vector and velocity vector of the satellite, then

$$\begin{aligned} \vec{Z}_T &= \frac{\vec{P}(t)}{\left\|\vec{P}(t)\right\|} \\ \vec{Y}_T &= \frac{\vec{V}(t) \times \vec{Z}_T}{\|\vec{V}(t) \times \vec{Z}_T\|} \\ \vec{X}_T &= \vec{Z}_T \times \vec{Y}_T \end{aligned} \tag{4}$$

where $\times$ represents the product of two vectors, and the transformation matrix R_{O2Ce} between the orbital coordinate system and the celestial coordinate system can be described as

$$R_{O2Ce} = \begin{bmatrix} (X_T)_X & (Y_T)_X & (Z_T)_X \\ (X_T)_Y & (Y_T)_Y & (Z_T)_Y \\ (X_T)_Z & (Y_T)_Z & (Z_T)_Z \end{bmatrix} \tag{5}$$

According to the above-mentioned equations, the exit vector of the pixel in the detector array can be expressed in the celestial coordinate system as

$$\vec{\text{LOS}}_{Ce} = \text{R}_{\text{O2Ce}} R_{S2O}(\text{pitch}, \text{roll}, \text{yaw}) R_{C2S}(\alpha, \beta, \gamma) \overrightarrow{\text{LOS}} \tag{6}$$

and

$$\overrightarrow{LOS}_{Ce} = \begin{bmatrix} X_{Ce} \\ Y_{Ce} \\ Z_{Ce} \end{bmatrix} = \begin{bmatrix} \cos\sigma\cos\delta \\ \cos\sigma\sin\delta \\ \sin\sigma \end{bmatrix} \tag{7}$$

where δ and σ are the star's right ascension and declination.

3) Stellar-Based Geometric Positioning Model: We can obtain the position coordinates (u, v) of the image stars using a centroid extraction algorithm; the azimuth θ, and the elevation φ of the pointing mirror by the measurement instruments; the installation angles α, β, and γ between the camera coordinate system and the satellite body coordinate system at the time of installation; and the instantaneous attitude angles of pitch, roll, and yaw and orbital parameters, namely, the instantaneous position vector $\vec{P}(t)$ and velocity vector $\vec{V}(t)$, by the attitude sensors. Then, the S-BGPM of the RSCs can be constructed from (1) to (7) as

$$\begin{aligned} \overrightarrow{\mathrm{LOS}_{ce}} = & \begin{bmatrix} \cos\sigma\cos\delta \\ \cos\sigma\sin \\ \sin\sigma \end{bmatrix} = \mathrm{R}_{O2Ce}\cdot R_{S2O}(\text{pitch, roll, yaw}) \\ & \cdot R_{C2S}(\alpha,\beta,\gamma)\cdot R_{\mathrm{Ref}}(\phi)\cdot R_{\theta}\cdot R_{\varphi} \\ & \cdot \begin{bmatrix} d_x & 0 & 0 \\ 0 & d_y & 0 \\ 0 & 0 & -f \end{bmatrix} \cdot \begin{bmatrix} u-u_0 \\ v-v_0 \\ 1 \end{bmatrix} \end{aligned} \tag{8}$$

where δ and σ represent the right ascension and declination, respectively; $\vec{\mathrm{LOS}}_{Ce}$ is the direction vector corresponding to the star's right ascension and declination in the celestial coordinate system.

Equation (8) is the S-BGPM from the star points in the pixel coordinate system to the right ascension and declination in the celestial coordinate system. Once the RSCs operate normally on -orbit, the accuracy and stability of $\mathrm{R_{O2Ce}}$, $R_{S2O}(\text{pitch, roll, yaw})$, $R_{\mathrm{Ref}}(\phi)$, R_{θ}, and R_{φ} mainly depend on the corresponding measurement devices that may inevitably introduce measurement errors. However, the installation matrix $R_{C2S}(\alpha,\beta,\gamma)$ and the distortion model determined before launch are able to change dramatically with the STD caused by the variation of the incident angle of the sunlight, which ultimately results in a significant impact on the positioning accuracy of RSCs and must be corrected.

4) Error Analysis: In general, the factors impacting the geometric positioning accuracy of spatial RSCs mainly consist of the measurement errors of the internal and external orientation parameters of the camera. The errors of the internal orientation parameters mainly include the coordinates error of the image points caused by the internal distortion of the optical system and the calibration error of the principal point and the principal distance; The errors of the external orientation parameters are mainly comprised of the deviation of the installation angle of the camera, the observation error of the attitude, and the orbital measurement error [4]. In addition, the centroid extraction error of the star points, the time synchronization error, the pointing error of the boresight caused by the shock and jitter of the satellite platform, and the positioning error caused by the STD are especially crucial for applications that involve super-accurate measurements such as geometric positioning of on-orbit RSCs.

The analysis shows that the pointing error of the boresight of the camera, the attitude observation error, and the orbital measurement error all contain systematic errors and random errors, where the error of the installation angle of the camera is primarily a systematic error. Generally, the systematic errors are accessible to measure and compensate by constructing an appropriate calibration model. However, the most effective method of the decreasing random errors is to use more precise instruments to improve the observation accuracy and reduce its influence. During the operation in orbit, the attitude observation error and the orbital measurement error change little with time and basically remain constant. However, the optical distortion model and the installation angle of the camera change dramatically because of the STD, and, consequently, leave a considerable effect on the positioning accuracy.

B. Correction Method

1) Error Representation: In this paper, the absolute positioning errors of the right ascension and declination directions and the total absolute positioning error are, respectively, defined as

$$\mathrm{RAerror} = \delta' - \delta \tag{9}$$

$$\mathrm{DEerror} = \sigma' - \sigma \tag{10}$$

$$\text{Total Error} = \sqrt{(\delta'-\delta)^2 + (\sigma'-\sigma)^2} \tag{11}$$

where δ' and σ' are the practical coordinates of the right ascension and declination of the stars corresponding to the star image points in the celestial coordinate system calculated by (8).δ and σ are the coordinates of the right ascension and declination of the stars determined from the star catalog according to the observation plan.

2) Model Fitting: Because of the rotation and revolution of the earth, the camera positioning error caused by STD exhibits short-period and long-period regular changes in relatively short- and long-time periods [20]. Theoretically, any periodic function that satisfies the Dirichlet conditions can be expanded into a Fourier series and can converge in the L^2-norm [33], [34]. The positioning error caused by STD is a function of the spatial temperature field which contains the Dirichlet conditions. Therefore, the Fourier series model (FSM) is appropriate to fit the positioning error.

In principle, the effectiveness of FSM can be better with an increase in order. However, an excessive order can not only increase the computational complexity but also multiply the model parameters and easily result in overfitting [34]. Therefore, this paper adopts a third-order FSM to fit the error variation as

$$\mathrm{FittingError} = a_0 + \sum_{i=1}^{3}\left(a_i\cos(i*\omega*T) + b_i\sin(i*\omega*T)\right) \tag{12}$$

where $a_0, a_1, b_1, a_2, b_2, a_3, b_3$, and$\omega$ are the model parameters, T is the time, and FittingError is the result of the fitting model.

Then, the least-square solution and the Levenberg–Marquardt (LM) algorithm are used to obtain the eight model

parameters a_0, a_1, b_1, a_2, b_2, a_3, b_3, and ω according to

$$\min_{N\geq 8} \sum_{i=1}^{N} d(\text{Total Error}, \text{FittingError})^2 \tag{13}$$

where $d(\text{Total Error}, \text{FittingError}) = \text{TotalError} - \text{FittingError}$ represents the fitting error of the model.

3) Correction Algorithm: Comparing to the low-orbit satellites, the operational temperature experienced by geostationary orbit satellites changes dramatically during a year. Consequently, the variation tendency of positioning error changes differently in different months, even in different days in some special months such as August. Long-term in-orbit observations suggest that the positioning errors of consecutive four days basically remain about the same. The positioning errors divided 5 days apart from each other are more different.

In fact, apart from the similarity in the neighboring days, the positioning errors caused by spatial thermal environment have no repeatability during a year. Moreover, the positioning errors in different years are also not reproducible because of the attenuation of instrument thermal control coating material. Based on the facts just mentioned, the positioning errors obtained in different times have its own traits. Therefore, it is not appropriate to divide the positioning errors into two parts, namely, the training and the test data sets, in the time dimension because of the special characteristics of the observation data.

Consequently, considering the influences of systematic errors and the minor changes of the positioning errors in a short continuous observation period, this paper uses a consecutive three-day fitting model to correct the positioning error for the following day. The specific correction algorithm is defined as follows.

For correction of positioning errors caused by STD, we assume that $F_1, F_2, \ldots, F_n$ are the third-order FSMs obtained by fitting the positioning errors $D_1, D_2, \ldots, D_n$ of the consecutive n days.

For the first two days, the fitting third-order FSM of F_1 is used as the final correction model $F_{cm1,2}$, namely, $F_{cm1,2} = F_1$, to correct the positioning errors of D_1 and D_2.

For the third day, we construct a new linear model as

$$F_{nl3} = q_0 + q_1 F_1 \tag{14}$$

where q_0 and q_1 are the model parameters and F_{nl3} is the new linear model. The q_0 and q_1 can be calculated with the positioning error of D_2 using a least-squares solution and the LM algorithm. Then, the final correction model is constructed as

$$F_{cm3} = q_0 + q_1 F_2 \tag{15}$$

where F_{cm3} is the final correction model and can be used to correct the positioning error D_3.

Similarly, for the -fourth day, we construct a new linear model as

$$F_{nl4} = q_0 + q_1 F_1 + q_2 F_2 \tag{16}$$

where q_0, q_1, and q_2 are the model parameters and F_{nl4} is the new linear model. q_0 and q_1 can be calculated with the positioning error of D_3 using a least-squares solution and the LM algorithm. Then, the final correction model is constructed as

$$F_{cm4} = q_0 + q_1 F_2 + q_2 F_3 \tag{17}$$

where F_{cm4} is the final correction model and can be used to correct the positioning error D_4.

For the other i-th day($i \geq 5$), the new linear model is constructed as

$$F_{nli} = q_0 + q_1 F_{i-4} + q_2 F_{i-3} + q_3 F_{i-2} \tag{18}$$

where q_0, q_1, q_2, andq_3 are the model parameters and F_{nli} is the new linear model. The q_0, q_1, q_2, and q_3 can be calculated with the positioning error of D_{i-1} using a least-squares solution and the LM algorithm. Then, the final correction model is constructed as

$$F_{cmi} = q_0 + q_1 F_{i-3} + q_2 F_{i-2} + q_3 F_{i-1} \tag{19}$$

where F_{cmi} is the final correction model and can be used to correct the positioning error $D_{i.}$.

The error after correction by this method can be expressed as

$$\text{Corrected Error} = \text{Total error} - F_{cm} \tag{20}$$

where Total error is the total positioning error of the camera; F_{cm} is the estimate value of the positioning error; Corrected Error is the corrected positioning error. A more detailed pseudocode of this method is shown in Algorithm 1.

Finally, a probability statistical method is used to study the probability distribution of the correction error and to evaluate the correction accuracy of this method.

TABLE I
PARAMETERS OF THE EXPERIMENT SATELLITE

Items	Detailed parameters
Orbit altitude	36000Km
Array sensor information	1024×1024 HgCdTe
Pixel size	25μm (short-wave infrared)
Focal length	1250mm (short-wave infrared)
Accuracy of attitude measurements	1×10^{-4} °/s

III. EXPERIMENTAL RESULTS

According to the proposed method, we exploited the real star observation short-wave infrared data of the staring camera of a geostationary experiment satellite based on the wide-field infrared survey explorer catalog to give an experimental verification. The observations were collected from August 1, 2017 to August 21, 2017. The detailed information of the experiment satellite was shown in Table I. The camera operates for 24 h a day. Data collected for the 21 consecutive days of

Algorithm 1 CA

Input: The positioning errors (data volume: n consecutive days of observation positioning errors);
Output: The corrected positioning errors (data volume: n consecutive days of corrected observation positioning errors);
1: **Set:** D = {D_1,D_2, . . ., D_n} ← The positioning errors of n consecutive days 1, 2, 3, . . . n (n > 0);
2: **Set:** F = {F_1,F_2, . . ., F_n} ← The obtained fitting third-order FSMs corresponding to the positioning errors of {D_1,D_2, . . ., D_n};
3: **for** i= 1 to n **do**
4: (Correcting the positioning errors of the first four days)
5: **if** $i < 5$ **then**
6: **if** $i < 3$ **then**
7: $F_{\text{nli}} = F_1$(The constructed new linear model);
8: $F_{\text{cmi}} = F_1$(The final correction model);
9: **else if** $i < 4$ **then**
10: $F_{\text{nli}} = q_0 + q_1F_1$ (The constructed new linear model);
11: Q = {q_0, q_1} ← The parameters q_0 and q_1 calculated with the positioning error D_2;
12: $F_{\text{cmi}} = q_0 + q_1F_2$ (The final correction model);
13: **end if**
14: **else**
15: $F_{\text{nli}} = q_0 + q_1F_1 + q_2F_2$ (The constructed new linear model);
16: Q = {q_0, q_1, q_2} ← The parameters q_0, q_1 and q_2 calculated with the positioning error D_3;
17: $F_{\text{cmi}} = q_0 + q_1F_2 + q_2F_3$ (The final correction model);
18: **end if**
19: $F_{\text{nli}} = q_0+q_1F_{i-4}+q_2F_{i-3}+q_3F_{i-2}$ (The constructed new linear model);
20: Q = {q_0, q_1, q_2, q_3} ← The parameters q_0, q_1, q_2 and q_3 calculated with the positioning error D_{i-1};
21: $F_{\text{cmi}} = q_0 + q_1F_{i-3} + q_2F_{i-2} + q_3F_{i-1}$(The final correction model);
22: Corrected error = $D_i - F_{\text{cmi}}$ (The corrected positioning errors of the observation data);
23: **end for**

August, 2017 was selected for the analysis of the positioning error caused by STD, and the experimental results are shown in the following.

A. Variation Tendency of Positioning Error

With the observation data from 21 consecutive days, the positioning error in the right ascension direction and the declination direction and the total positioning error of the RSC are solved by (8),,0–(11). After eliminating the systematic deviation, the variation tendency of each positioning error with relative time beginning at 00:00:00 of the first day is shown in Fig. 3.

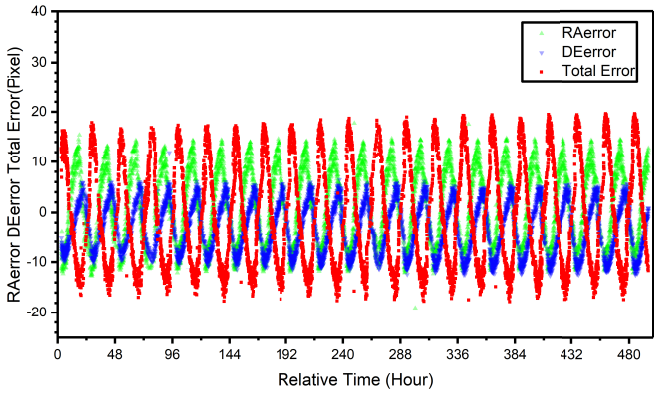

Fig. 3. Variation tendency of the positioning error. The green triangle, blue inverted triangle, and the red square represent the positioning error in the right ascension direction, the positioning error in the declination direction, and the total positioning error, respectively.

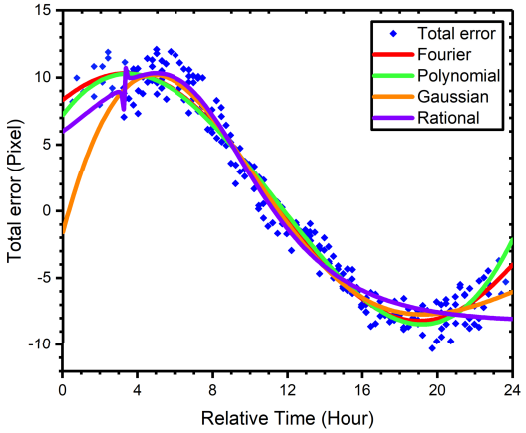

Fig. 4. Comparison of models. The blue squares are the data points of the total positioning errors. The red, green, orange, and purple curves are the fitting results with the third-order FSM, PM, GM, and RFFM, respectively.

Obviously, except for some outlying points, the three types of positioning errors fluctuate regularly with a period of about 24 h, indicating that the geostationary orbit optical payload positioning error caused by STD varies approximately in a cycle of a day. Moreover, comparing the tendency of the 21-day positioning error, it is not difficult to find that the amplitude of the positioning error is relatively stable over a short time, except for the influence of random errors. Subtracting the systematic errors of the RSC, the positioning error before correction is approximately within ±18 pixels.

B. Fitting Analysis

Taking the selected 21-day consecutive data for an example, we fit the positioning errors with a third-order FSM, third-order polynomial model (PM), third-order Gaussian model (GM), and third-order rational fractional function model (RFFM), respectively. The following equation shows the expression of the third-order RFFM:.

$$\text{Fittingresults}_{\text{RFFM}} = \frac{a_1T^3 + a_2T^2 + a_3T + a_4}{T^3 + b_1T^2 + b_2T + b_3} \quad (21)$$

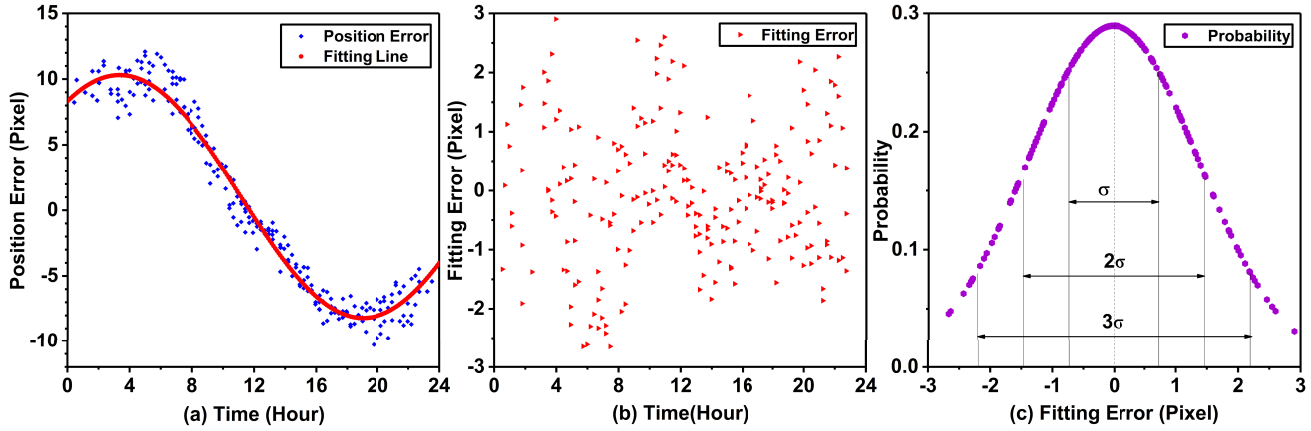

Fig. 5. (a) Fitting results of the third-order FSM. (b) Distribution of fitting error. (c) Probability distribution of fitting error.

TABLE II
ANALYSIS OF FITTING ACCURACY OF DIFFERENT MODELS

Fitting Model	Numbers of Coefficients	R-Square	RMSE
3-FSM	8	0.97	1.119
3-PM	4	0.9597	1.3
3-GM	9	0.9616	1.484
3-RFFM	7	0.9607	1.394

R-Square is the determination coefficient of the models, and the closer the R-Square approaches 1, the better the fitting effectiveness becomes.

TABLE III
ANALYSIS OF THE PROBABILITY DISTRIBUTION FOR THE FITTING ERROR

	CL	$\hat{\mu}$	CI of $\hat{\mu}$	$\hat{\sigma}$	CI of $\hat{\sigma}$
Fitting error	95%	8.6625×10^{-5}	(−0.1087, 0.1087)	0.7310	(0.6854, 0.8157)

CL and CI are the confidence level and confidence interval. $\hat{\mu}$ and $\hat{\sigma}$ are the estimate value of the mean and the standard deviation.

where a_1, a_2, a_3, a_4, b_1, b_2, and b_3 are the parameters of the RFFM, T is the time, and $\text{Fittingresults}_{\text{RFFM}}$ is the result of the fitting model. Accordingly, the fitting results of the first day are derived as follows.

As shown in Fig. 4, the third-order FSM and the third-order PM can better fit the error tendency of the first day than the third-order GM and the third-order RFFM. The error data points are distributed evenly around the fitted curve. Moreover, it should be noted from Table II that the third-order FSM has a smaller root-mean-squared error (RMSE) and a larger determination coefficient of R-Square than the third-order PM. Therefore, the third-order FSM should be more appropriate for fitting the error points.

The variation tendency of the error for a specific day has been fitted with the third-order FSM as mentioned above. The fitting results, the distribution of the fitting error, and the probability distribution of the fitting error analyzed with a normal distribution method are shown in Fig. 5(a),–(c), respectively. It can be seen from Fig. 5(b) that the fitting error of three-order FSM is generally distributed within ±3 pixels. The probability distribution in Fig. 5(c) and Table III reveals that the probability of the fitting error being no more than ±1.5 pixels at a 95% confidence level, can be 95.44% (2σ).

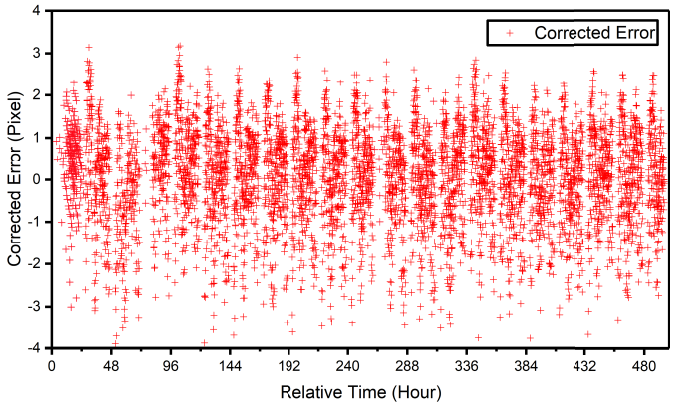

Fig. 6. Distribution of the corrected error.

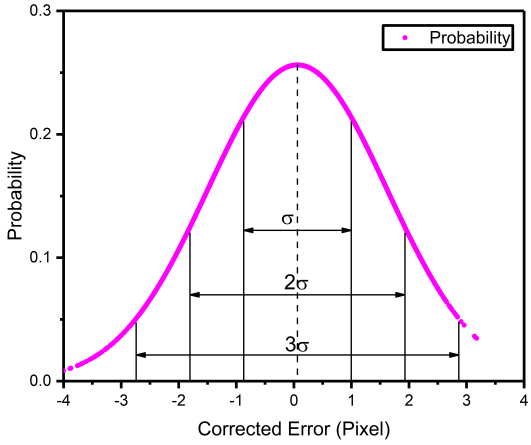

Fig. 7. Probability distribution of the correction error.

C. Correction Results

With the correction method proposed in Section II, we have corrected the positioning error of the 21 days shown in Fig. 3 and presented the distribution of the correction error in Fig. 6. It can be clearly seen that the correction positioning error is generally distributed within ±3 pixels, which is greatly improved compared to the former error of ±18 pixels without correction.

TABLE IV
ANALYSIS OF THE PROBABILITY DISTRIBUTION FOR CORRECTED ERROR

	CL	$\hat{\mu}$	CI of $\hat{\mu}$	$\hat{\sigma}$	CI of $\hat{\sigma}$
Corrected error	95%	0.0619	(0.0213, 0.1026)	0.9341	(0.9172, 0.9517)

CL and CI are the confidence level and confidence interval. $\hat{\mu}$ and $\hat{\sigma}$ are the estimate value of the mean and the standard deviation.

Similarly, the normal distribution method is adopted to explore the probability distribution of the correction positioning error, and the results are shown in Fig. 7 and TABLE III. Obviously, the probability of the correction error being no more than ± 1.9 pixels at a 95% confidence level, can be 95.44% (2σ) as shown in Fig. 7 and Table IV.

It should be noted that the distribution of the correction error is continuous but not uniform on the horizontal axis, which implies the uniformity of the original data. The uniformity and continuity of the original error data can be one of the most significant factors that affect the accuracy of the fitting model and the correction results. In addition, the accuracy of centroid extraction for the selected stars fundamentally determines the positioning accuracy of the proposed S-BGPM. Improvement of the centroid extraction precision can directly improve the positioning accuracy of the camera, and can effectively reduce the impact of STD.

IV. CONCLUSION

In this paper, a novel correction method for correcting the positioning error caused by STD is proposed. The S-BGPM from the star points of the images in the pixel coordinate system to the right ascension and declination in the celestial coordinate system and the correction method that uses the linear combination of the consecutive three-day fitting models to correct the positioning error for the following day are constructed. Experimental results show that the proposed method can effectively correct the positioning error caused by STD and provide the possibility of long-term continuous observation for geostationary orbiting staring cameras. Although this geometric positioning model is proposed for calculating the position coordinates of the observed stars for a certain type of RSC, it is still suitable and versatile for the other high-altitude RSCs because the spatial relationship between the camera imaging mechanism and the position determining instruments is basically similar.

REFERENCES

[1] J. Jia *et al.*, "High spatial resolution shortwave infrared imaging technology based on time delay and digital accumulation method," *Infr. Phys. Technol.*, vol. 81, pp. 305–312, Mar. 2017.

[2] J. Liang, Z. Yang, J. Zhang, and Y.-Z. Luo, "Formation establishment for GEO satellite beams monitoring using controlled regressive orbits," *Acta Astronautica*, vol. 150, pp. 213–222, Sep. 2018.

[3] P. Zhou, L. Du, X. Li, and Y. Gao, "Near real-time BDS GEO satellite orbit determination and maneuver analysis with reversed point positioning," *Adv. Space Res.*, vol. 63, no. 5, pp. 1781–1791, Mar. 2019.

[4] Y. Liu, L. Yang, and F.-S. Chen, "Multispectral registration method based on stellar trajectory fitting," *Opt. Quantum Electron.*, vol. 50, no. 4, p. 189, Apr. 2018.

[5] W. Lyu, T. Wang, Y. Dong, and Y. Shen, "Imaging navigation and registration for geostationary imager," *IEEE Geosci. Remote Sens. Lett.*, vol. 14, no. 12, pp. 2175–2179, Dec. 2017.

[6] J. L. Fiorello, I. H. Oh, K. A. Kelly, and L. Ranne, "GOES I/M image navigation and registration," in *Proc. Flight Mech./Estimation Theory Symp.*, 1989, pp. 129–147.

[7] S.-F. Tian and J. Li, "An efficient method for measuring the internal parameters of optical cameras based on optical fibres," *Sci. Rep.*, vol. 7, no. 1, Sep. 2017, Art. no. 12479.

[8] De Lussy *et al.*, "Pleiades HR in flight geometrical calibration: Location and mapping of the focal plane," *Int. Arch. Photogramm. Remote Sens. Spat. Inf. Sci.*, vol. 39, pp. 519–523, Jul. 2012.

[9] D. Mulawa, "On-orbit geometric calibration of the OrbView-3 high resolution imaging satellite," *Int. Arch. Photogramm. Remote Sens. Spatial Inf. Sci.*, vol. 35, pp. 1–6, Jul. 2004.

[10] P. V. Radhadevi and S. S. Solanki, "In-flight geometric calibration of different cameras of IRS-P 6 using a physical sensor model," *Photogramm. Rec.*, vol. 23, no. 121, pp. 69–89, Mar. 2008.

[11] P. V. Radhadevi, M. Rupert, D. Pablo, and P. Reinartz, "In-flight geometric calibration and orientation of ALOS/PRISM imagery with a generic sensor model," *Photogramm. Eng. Remote Sens.*, vol. 77, no. 5, pp. 531–538, May 2011.

[12] S. Leprince, P. Mus, and J.-P. Avouac, "In-flight CCD distortion calibration for pushbroom satellites based on subpixel correlation," *IEEE Trans. Geosci. Remote Sens.*, vol. 46, no. 9, pp. 2675–2683, Sep. 2008.

[13] H. Topan and D. Maktav, "Efficiency of orientation parameters on georeferencing accuracy of SPOT-5 HRG level-1A stereoimages," *IEEE Trans. Geosci. Remote Sens.*, vol. 52, no. 6, pp. 3683–3694, Jun. 2014.

[14] M. Wang, Y. Zhu, S. Jin, J. Pan, and Q. Zhu, "Correction of ZY-3 image distortion caused by satellite jitter via virtual steady reimaging using attitude data," *ISPRS J. Photogram. Remote Sens.*, vol. 119, pp. 108–123, Sep. 2016.

[15] A. Iwasaki, "Detection and estimation satellite attitude jitter using remote sensing imagery," in *Advances in Spacecraft Technologies*. Rijeka, Croatia: InTech, 2011.

[16] W. Yue-Ming, "An advanced scanning method for space-borne hyper-spectral imaging system," *Proc. SPIE*, vol. 8196, Aug. 2011, Art. no. 819626.

[17] T. Wang, "Geometric accuracy validation for ZY-3 satellite imagery," *IEEE Geosci. Remote Sens. Lett.*, vol. 11, no. 6, pp. 1168–1171, Jun. 2014.

[18] Y. Zhang, M. Zheng, J. Xiong, Y. Lu, and X. Xiong, "On-orbit geometric calibration of ZY-3 three-line array imagery with multistrip data sets," *IEEE Trans. Geosci. Remote Sens.*, vol. 52, no. 1, pp. 224–234, Jan. 2014.

[19] Y. Zhang, M. Zheng, X. Xiong, and J. Xiong, "Multistrip bundle block adjustment of ZY-3 satellite imagery by rigorous sensor model without ground control point," *IEEE Geosci. Remote Sens. Lett.*, vol. 12, no. 4, pp. 865–869, Apr. 2015.

[20] M. Wang, Y. Cheng, X. Chang, S. Jin, and Y. Zhu, "On-orbit geometric calibration and geometric quality assessment for the high-resolution geostationary optical satellite GaoFen4," *ISPRS J. Photogramm. Remote Sens.*, vol. 125, pp. 63–77, Mar. 2017.

[21] M. Wang, Y. Cheng, Y. Tian, L. He, and Y. Wang, "A new on-orbit geometric self-calibration approach for the high-resolution geostationary optical satellite GaoFen4," *IEEE J. Sel. Topics Appl. Earth Observ. Remote Sens.*, vol. 11, no. 5, pp. 1670–1683, May 2018.

[22] B. Yang, Y. Pi, X. Li, and M. Wang, "Relative geometric refinement of patch images without use of ground control points for the geostationary optical satellite GaoFen4," *IEEE Trans. Geosci. Remote Sens.*, vol. 56, no. 1, pp. 474–484, Jan. 2017. doi: 10.1109/TGRS.2017.2750320.

[23] L. Vaillon, U. Schull, T. Knigge, and C. Bevillon, "Geo-oculus: High resolution multi-spectral earth imaging mission from geostationary orbit," *Proc. SPIE*, vol. 10565, Nov. 2017, Art. no. 105651V.

[24] J. A. Moody, "SBIRS Background. Achieving affordable operational requirements on the SBIRS program," *AU/ACSC*, vol. 548, pp. 5–12, Mar. 1997.

[25] J. Chen, W. An, X. Deng, J. Yang, and Z. Sha, "Space based optical staring sensor LOS determination and calibration using GCPs observation," *Proc. SPIE*, vol. 9987, Oct. 2016, Art. no. 99870Y.

[26] C. Wheeler, T. Walsh, and A. Krimchansky, "Strategies to maximize science data availability for the GOES-R series of satellites," in *Proc. SpaceOps Conf.*, May 2018, p. 2577.

[27] S. Houchin, B. Porter, J. Graybill, and P. Slingerland, "Image navigation and registration performance assessment evaluation tools for GOES-R ABI and GLM," in *Proc. IEEE Int. Geosci. Remote Sens. Symp. (IGARSS)*, Fort Worth, TX, USA, Jul. 2017, pp. 2074–2077.

[28] J. Weng, P. Cohen, and M. Herniou, "Camera calibration with distortion models and accuracy evaluation," *IEEE Trans. Pattern Anal. Mach. Intell.*, vol. 14, no. 10, pp. 965–980, Oct. 1992.

[29] F. Remondino and C. Fraser, "Digital camera calibration methods: Considerations and comparisons," *Int. Arch. Photogramm., Remote Sens. Spatial Inf. Sci.*, vol. 36, no. 5, pp. 266–272, Sep. 2006.
[30] C. S. Fraser, "Digital camera self-calibration," *ISPRS J. Photogramm. Remote Sens.*, vol. 52, pp. 149–159, Aug. 1997.
[31] F. Yilmaztürk, "Full-automatic self-calibration of color digital cameras using color targets," *Opt. Express*, vol. 19, no. 19, pp. 18164–18174, Sep. 2011.
[32] M. Wang, Y. Cheng, B. Yang, S. Jin, and H. Su, "On-orbit calibration approach for optical navigation camera in deep space exploration," *Opt. Express*, vol. 24, no. 5, pp. 5536–5554, Mar. 2016.
[33] J. Kannala and S. S. Brandt, "A generic camera model and calibration method for conventional, wide-angle, and fish-eye lenses," *IEEE Trans. Pattern Anal. Mach. Intell.*, vol. 28, no. 8, pp. 1335–1340, Aug. 2006.
[34] E. B. Brooks, V. A. Thomas, R. H. Wynne, and J. W. Coulston, "Fitting the multitemporal curve: A Fourier series approach to the missing data problem in remote sensing analysis," *IEEE Trans. Geosci. Remote Sens.*, vol. 50, no. 9, pp. 3340–3353, Sep. 2012.

Xiaoyan Li received the B.S. degree in mechanism design, manufacturing, and automatization from Northwest A&F University, Xi'an, China, in 2016. He is currently pursuing the Ph.D. degree in electronic circuit and system with the Shanghai Institute of Technical Physics, Chinese Academy of Sciences, University of Chinese Academy of Sciences, Beijing, China.

His research interests include on-orbit accurate navigation and geometric calibration of remote sensing satellites.

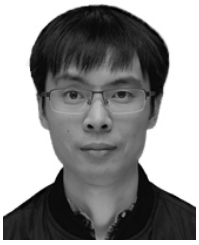

Lin Yang received the B.S. degree in optical information science and technology from the Chongqing University of Posts and Telecommunications, Chongqing, China, in 2005, and the Ph.D. degree in optics from the Changchun Institute of Optics, Fine Mechanics and Physics, Chinese Academy of Sciences, Changchun, China, in 2011.

His research interests include design of infrared remote sensing payloads, including the optical design of high temporal and spatial resolution infrared remote sensing payloads, low-temperature optical payloads assembly and testing technology, and the ground and on-orbit calibration of infrared remote sensing cameras.

Xiaofeng Su received the B.S. degree in electronic engineering from Xiamen University, Xiamen, China, in 2010, and the Ph.D. degree in electronic circuit and system from the Shanghai Institute of Technical Physics, Chinese Academy of Sciences, Shanghai, China, in 2015.

His research interests include the design of infrared remote sensing payloads, including the information acquisition and processing technology of large-array detector components with large dynamic range and low-noise, infrared weak target detection and tracking technology.

Zhuoyue Hu received the B.S. degree in information display and opto-electronic technology from the University of Electronic Science and Technology of China, Chengdu, China, in 2016. She is currently pursuing the Ph.D. degree in physical electronics with the Shanghai Institute of Technical Physics of the Chinese Academy of Sciences, University of Chinese Academy of Sciences, Beijing, China.

Her research interests include radiometric calibration of remote sensing satellites.

Fansheng Chen received the B.S. degree in opto-electronic information engineering from Shandong University, Jinan, China, in 2002, and the Ph.D. degree in physical electronics from the Shanghai Institute of Technical Physics of the Chinese Academy of Sciences, Shanghai, China, in 2007.

Since 2013, he has been a Professor with the Shanghai Institute of Technical Physics of the Chinese Academy of Sciences. His research interests include the design of spatial high-resolution remote sensing and detection payloads, high-speed and low noise information acquisition technology, and infrared dim small target detection technology. Meanwhile, he has been committed to the research and development of the space infrared staring detection instruments, the high spatial and temporal resolution photoelectric payloads, and the application of infrared multi-spectral information acquisition technology in artificial intelligence, target recognition, and other relative aspects.